Journal of Materials Chemistry B

ROYAL SOCIETY OF CHEMISTRY

PAPER

View Article Online
View Journal | View Issue

Cite this: J. Mater. Chem. B, 2024, 12, 5377

An injectable hydrogel dressing for controlled release of hydrogen sulfide pleiotropically mediates the wound microenvironment†

Junwei Yang,‡[a] Xianzhen Dong,‡[a] Wenying Wei,‡[a] Kun Liu,[a] Xiaopei Wu[a] and Honglian Dai *[ab]

Received 27th February 2024,
Accepted 25th April 2024

DOI: 10.1039/d4tb00411f

rsc.li/materials-b

The healing of scalded wounds faces many challenges such as chronic inflammation, oxidative stress, wound infection, and difficulties in vascular and nerve regeneration. Treating a single problem cannot effectively coordinate the complex regenerative microenvironment of scalded wounds, limiting the healing and functional recovery of the skin. Therefore, there is a need to develop a multi-effect treatment plan that can adaptively address the issues at each stage of wound healing. In this study, we propose a scheme for on-demand release of hydrogen sulfide (H_2S) based on the concentration of reactive oxygen species (ROS) in the wound microenvironment. This is achieved by encapsulating peroxythiocarbamate (PTCM) in the ROS-responsive polymer poly(ethylene glycol)–poly(L-methionine) (PMet) to form nanoparticles, which are loaded into a thermosensitive injectable hydrogel, F127-poly(L-aspartic acid-*N*-hydroxysuccinimide) (F127-P(Asp-NHS)), to create a scald dressing. The H_2S released by the hydrogel dressing on demand regulates the wound microenvironment by alleviating infection, reducing oxidative stress, and remodeling inflammation, thereby accelerating the healing of full-thickness scalded wounds. This hydrogel dressing for the adaptive release of H_2S has great potential in addressing complex scalded wounds associated with infection and chronic inflammation.

1. Introduction

Burns and scalds, resulting in more than 180 000 annual fatalities globally, necessitate significant attention and specialized care.[1] According to the severity of the injury, burns and scalds can be categorized into three classes: first-degree, second-degree, and third-degree.[2] Scalded wounds are characterized by irregularity, severe fluid exudation, susceptibility to infection, and slow healing, thereby posing challenges in their management and imposing significant economic and psychological burdens on patients.[3] Scalded wound healing is a complex physiological process consisting of multiple stages.[4] One of the primary factors contributing to the challenging healing process of scalded wounds is the presence of prolonged and excessive inflammation, as supported by previous studies.[5,6] The local inflammatory response mediated by innate immune cells is triggered immediately after the formation of the scalded wound and macrophages are attracted to the injury site by various chemokines to maintain the acute inflammatory reaction, which could prevent infection and clear necrotic cells.[7] However, during scald healing, factors of pro-inflammation dominated the inflammatory balance, resulting in difficulties in polarization of macrophages to M2 phenotype, leading to long-term inflammation and complications.[8–10] At the same time, due to the accumulation of a mass of M1 macrophages in the wound, excess ROS are produced, causing oxidative stress. Long-term inflammation and oxidative stress hinder the regeneration of blood vessels and nerves and delay the speed of wound healing.[6,11–13]

Nitric oxide (NO),[14] carbon monoxide (CO),[15] and hydrogen sulfide (H_2S)[14] play a variety of roles in biological processes. H_2S has long been recognized as a toxic gas. However, in 1989, researchers made a significant discovery when they found endogenous H_2S in the human brain.[16] This discovery prompted further investigation into the physiological function of H_2S.[17–19] Due to its function as a gas transmitter and molecular target, H_2S holds significant potential for various applications such as anti-inflammation, anti-tumor, anti-apoptosis, and vasodilator effects.[20–24] Furthermore, H_2S, as

[a] State Key Laboratory of Advanced Technology for Materials Synthesis and Processing, Biomedical Materials and Engineering Research Center of Hubei Province, Wuhan University of Technology, Wuhan 430070, China. E-mail: daihonglian@whut.edu.cn
[b] Wuhan University of Technology Advanced Engineering Technology Research Institute of Zhongshan City, Zhongshan 528400, China

† Electronic supplementary information (ESI) available. See DOI: https://doi.org/10.1039/d4tb00411f

‡ These authors contributed equally to this work.

an exceedingly dynamic molecule, readily undergoes reactions with ROS.[23] PTCM is a class of H_2S donors that can be triggered by cellular ROS, and has the ability to release H_2S in the microenvironment with high ROS of scalded wounds.[25] The release of H_2S can effectively mitigate oxidative stress and alleviate inflammation.

Wound dressings, such as rubber,[26,27] membranes,[28–30] foam,[31,32] electrospun nanofibers,[33,34] and hydrogels,[35–37] play an important role in scald care.[38–40] A hydrogel, which is a hydrophilic polymer material with a three-dimensional network, can be formed through physical or chemical crosslinking. These characteristics enable it to absorb exudate tissue fluid and maintain permeability of oxygen and water, and a moist wound environment, which is conducive to wound healing.[3,41–43] In the face of irregular and deep scalded wound, injectable hydrogels can be injected into the wound, then form a complete hydrogel to fill the wound site to control wound infection and deliver drugs.[2,44] Therefore, the use of injectable hydrogels as matrix materials to design scald dressings has a good application prospect. Due to their excellent biocompatibility and biodegradability,[45,46] F127 and poly(aspartic acid) (PAsp) have been widely used and can serve as matrix materials for injectable hydrogels. H_2S-releasing hydrogel dressings have also been used in previous studies, such as near-infrared stimulation[47] and pH-responsive hydrogel dressings,[6] but the H_2S release in these studies was not timely and accurate in response to changes in the wound microenvironment. Therefore, it is necessary to develop a H_2S-releasing hydrogel dressing that can be multi-effective and accurately regulate the wound microenvironment during the whole cycle of wound healing.

In the present study, we introduce an "intelligent warehouse" system for H_2S delivery with ROS-triggered and on-demand release specifically designed for scalded wounds (Fig. 1). PTCM was encapsulated utilizing nanoparticles composed of poly(ethylene glycol)–poly(L-methionine) (mPEG-PMet) to form PTCM@PMet nanoparticles (PTCM@PMet NPs). The NPs were incorporated into a thermosensitive hydrogel, more specifically, the precursor solution of F127-poly(L-aspartic acid-*N*-hydroxysuccinimide) (F127-P(Asp-NHS)), which will undergo *in situ* gelation under body temperature upon injection into the scalded wound. Subsequently, the build-up of ROS caused by ischemia and inflammation at the wound site will disrupt the PTCM@PMet NPs and stimulate H_2S release. *In vitro* studies have shown that H_2S released at an appropriate level could inhibit bacterial growth and induce macrophage polarization toward the M2 phenotype, promote the migration and tube formation of human umbilical vein endothelial cells (HUVECs), and reduce oxidative stress in the rat Schwann cell (RSC) oxidative damage model. *In vivo* experiments have demonstrated that the application of PTCM@PMet NPs/F127-P(Asp-NHS) dressing effectively promotes the scald healing and functional recovery of skin. These results suggest that the implementation of this strategy has the potential to generate novel approaches for the treatment of various types of challenging wounds that are slow to heal.

2. Methods

2.1. Materials

Pluronic F127 (M_n = 12 600), stannic oxide ($Sn(Oct)_2$) and ε-caprolactone were obtained from Sigma-Aldrich. Methoxy

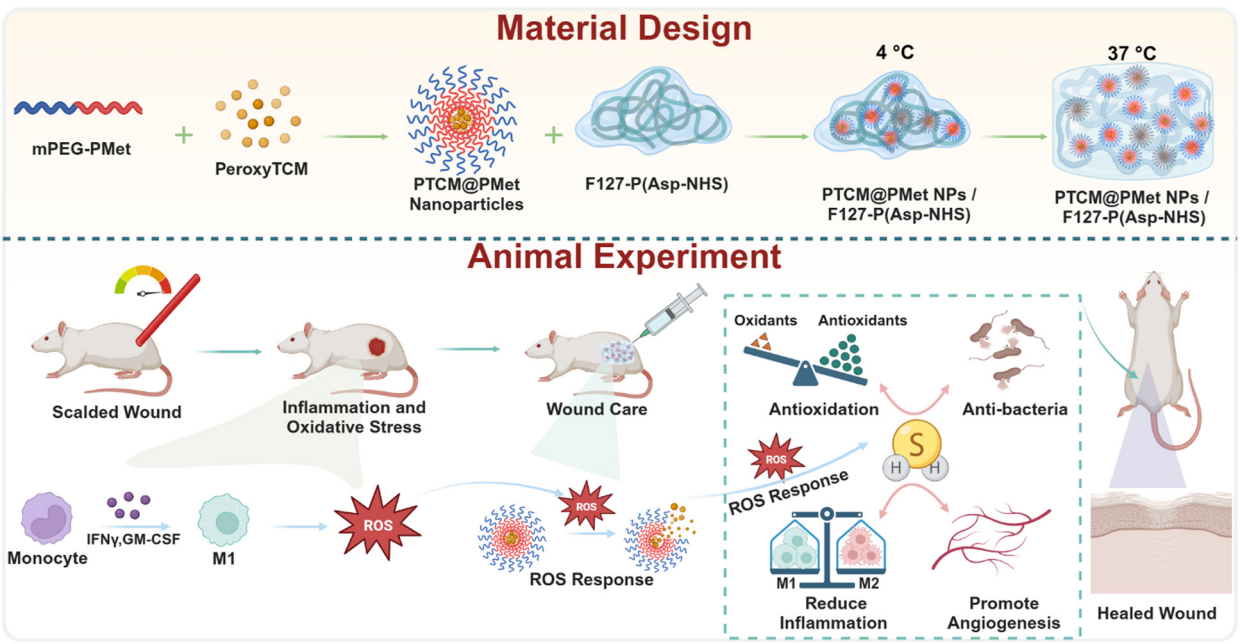

Fig. 1 Schematic diagram of an "intelligent warehouse" of H_2S skin dressing for scalded wound repair. After a scald, inflammation and possible infection can generate a large amount of ROS, triggering the release of H_2S donors from the PTCM@PMet NPs and further the production of H_2S. H_2S has functions such as antioxidation, anti-inflammation, antibacterial, and promotion of neurovascular regeneration, which can accelerate the reconstruction of the scalded wound microenvironment, promote wound healing, and restore skin structure.

poly(ethylene glycol) (mPEG2000) was acquired from Tokyo Chemical Industry (TCI, Shanghai). 4-Fluorophenyl isothiocyanate, 4-(hydroxymethyl)phenylboronic acid pinacol ester, calcium hydride (CaH_2), dimethyl sulfoxide-d_6 (DMSO-d_6), acetonitrile-d_3 (CD_3CN), deuterium oxide (D_2O), trichloromethane-d ($CDCl_3$), sodium hydride (NaH), sodium (Na), methionine, triphosgene, 1-(3-dimethylaminopropyl)-3-ethylcarbodiimide hydrochloride (EDC), *N*-hydroxysuccinimide (NHS), and *p*-toluenesulfonyl were obtained from Shanghai Aladdin Biochemical Technology Co., Ltd. L-Aspartic acid 4-benzyl ester was acquired from Energy Chemical. Ammonium chloride (NH_4Cl), tetrahydrofuran (THF), chloroacetyl chloride, aqueous ammonia ($NH_3 \cdot H_2O$) (aq), ethyl acetate (EA), dimethyl sulfoxide (DMSO), *N*,*N*-dimethylformamide (DMF), anhydrous ether, dichloromethane (DCM), toluene, trichloromethane ($CHCl_3$), methanol, triethylamine, NaCl, and anhydrous $MgSO_4$ were obtained from Sinopharm Chemical Reagent Co., Ltd. CCK8 (40203ES60) was purchased from Yeasen Biotechnology (Shanghai) Co., Ltd. Brine and 2,7-dichlorodihydrofluorescein diacetate (DCFH-DA) (CA1410) were obtained from Solarbio (China).

2.2. Synthesis and characterization of PTCM

The PTCM compound was synthesized by combining 4-fluorophenyl isothiocyanate (10 mmol) and 4-(hydroxymethyl)phenylboronic acid pinacol ester (10 mmol) in anhydrous THF (20 mL) at 0 °C. NaH (12.5 equivalents (equiv.)) was subsequently added. After 20 min, the reaction was stirred at room temperature (r.t.) until the reaction was complete through observation of thin layer chromatography (TLC). Then, in order to stop the reaction, the brine (40 mL) was added to the solution, and the mixed solution was extracted with EA (3 × 20 mL). The organic layer was collected and dried overnight by adding $MgSO_4$, and the crude product was obtained by pumping and filtering followed by rotary evaporation. The crude product was purified by silica gel chromatography using EA and hexane as eluents. The chemical structure and molecular weight information was acquired using ^{1}H NMR and atmospheric pressure chemical ionization (APCI) techniques. ^{1}H NMR (500 MHz, chloroform-d) δ 8.26 (s, 1H), 5.61 (s, 2H), 1.35 (s, 12H). HRMS *m*/*z* [M + H]+ calcd for $[C_{20}H_{24}BFNO_3S]^+$ 388.291; found 388.154.

2.3. Evaluation of the ROS-responsiveness of PTCM to release H_2S

PTCM was introduced into a solution of CD_3CN and D_2O (1 : 1) that also contained H_2O_2 (5 equiv.). The release of H_2S was detected through the observation of temporal changes in the molecular structure using ^{1}H NMR spectroscopy.

2.4. Synthesis of PTCM@PMet NPs

A solution was prepared by dissolving 100 mg of PTCM and 100 mg of mPEG-PMet in 6 mL of DMF in a centrifuge tube. The solution was vigorously stirred while slowly adding 12 mL of deionized water from a syringe. After the completion of the deionized water drops, the mixed solution in centrifuge tube underwent a 24 h dialysis process in a dialysis bag with a molecular weight cut-off (MwCO) of 3500 Da to eliminate excess drug aggregates. The PTCM@PMet NPs were obtained through the process of freeze-drying. The determination of the drug content in the micelle was conducted using a UV spectrometer. PTCM@PMet NPs were dissolved in a mixed solution of DMSO and water (9 : 1), and the absorbance at 275 nm was measured. The drug content was then calculated using the standard curve. The mean hydrodynamic diameter and size distribution of the NPs were determined using DLS (Zetasizer Nano ZS, Malvern Instruments, UK). The morphology of the NPs was observed using a JEM-1400Plus transmission electron microscope (TEM, JEOL, Japan).

2.5. Synthesis of F127-P(Asp-NHS)

2 g of F127-NH_2 (1 equiv.) were introduced into a single-necked flask and subjected to vacuum drying at 80 °C in an oil bath for a duration of 2 h. Following cooling to r.t., 50 mL of anhydrous DMF was added, along with 1.1286 g of Asp NCA (30 equiv.), and the reaction was stirred under argon protection for three days. The reaction was settled with 500 mL ice ether, the solid was subjected to vacuum filtration, dissolved in DMF, and dialyzed with deionized water for three days, and F127-PBla was obtained by freeze-drying. 1 g of F127-PBla was dissolved in 6 mL of trifluoroacetic acid. Subsequently, 3 mL of hydrogen bromide was slowly added. The resulting mixture was stirred at r.t. for 30 min. The product was then precipitated using cold ether, dissolved in DMF, and subjected to dialysis with deionized water for three days using a dialysis bag (MwCO: 120 000 Da). Finally, the product was lyophilized to yield F127-PAsp. Finally, to endow the hydrogel with tissue adhesion ability, *N*-hydroxysuccinimide (NHS) groups are introduced into its side chain, which can react with amino groups in the tissue to form amide bonds.[48] 1 g of F127-PAsp, along with 0.1354 g of NHS and 0.6170 g of EDC, was dissolved in 50 mL of DMF. The mixture was stirred at r.t. for a period of three days. Afterward, it was settled using ice-cold diethyl ether, followed by dialysis with deionized water for three days using a dialysis bag (MwCO: 120 000 Da). Finally, the solution was lyophilized to obtain F127-P(Asp-NHS). F127-PBla ^{1}H NMR (500 MHz, TFA-d) δ 7.83–7.51 (m, 230H), 5.64–5.38 (m, 92H), 4.24 (s, 995H), 3.37 (s, 92H), 1.68–1.57 (m, 195H). F127-PAsp ^{1}H NMR (500 MHz, TFA-d) δ 4.22 (s, 995H), 3.34 (s, 13H), 1.61 (*t*, *J* = 8.1 Hz, 195H). F127-P(Asp-NHS) ^{1}H NMR (500 MHz, TFA-d) δ 4.23 (s, 995H), 3.48 (s, 14H), 1.67–1.57 (m, 195H).

2.6. Phase transition and rheological properties of the F127-P(Asp-NHS) hydrogels

Using the test tube inversion method, the sol–gel transition temperature of the F127-P(Asp-NHS) hydrogel was studied. The sol–gel critical phase transition temperature and rheological properties were then measured using a HAAKE RheoStress 6000 rotational rheometer (Thermo Scientific, Germany).

2.7. Plate counting of bacteria

The antibacterial effect of PTCM@PMet NPs examined through direct contact with *E. coli* and *S. aureus* bacteria. The cryopreserved solutions of bacteria were introduced into conical flasks

containing bovine upper brain extract. Subsequently, the bacteria were resuscitated by subjecting the flasks to agitation on a shaker for a duration of 24 h. The resuscitated bacterial solution was co-incubated for 24 h at 37 °C in a medium containing PTCM@PMet NPs and H_2O_2 (50 μM). PBS, PTCM@PMet NPs (50 μM), and H_2O_2 (50 μM) were used as control samples. The bacterial suspension was subsequently diluted using PBS (pH 7.4, 0.01 M) buffer and then inoculated onto a Petri dish containing solid medium.[49] After incubating at a temperature of 37 °C for a period of 12 h to 18 h, the total number of colonies was determined. All the aforementioned tests were conducted three times.

2.8. Cell culture

HUVECs and L929 cells were separately incubated in F-12K medium (Gibco, USA) and 1640 medium (Gibco, USA). RSCs and RAW 264.7 cell lines were cultured in DMEM (HyClone, USA). All media were supplemented with 10% fetal bovine serum (FBS, Gibco, USA) and 1% penicillin/streptomycin (PS, Gibco, USA). All cells were incubated in an atmosphere consisting of 95% air and 5% CO_2 at a temperature of 37 °C.

2.9. Cell viability assay

L929 cells were seeded in 96-well plates (5000 cells per well). Subsequently, the cells were incubated with PTCM (25 μM, 50 μM, and 100 μM) and PTCM@PMet NPs (25 μM, 50 μM, and 100 μM effective PTCM concentrations) for 1 and 3 days, and incubated with NaHS (25 μM, 50 μM, 100 μM, 200 μM, 400 μM, 800 μM, and 1600 μM) for 1 day. After washing with PBS, 200 μL PBS-free medium containing 10% CCK-8 was added and incubated for 2 h in an incubator. After shaking in the dark for 10 min, a 100 μL solution was sucked and added to a new 96-well plate, and the absorbance at 450 nm was measured using a microplate reader (Multiskan GO, Thermo Scientific, USA).

2.10. Intracellular imaging of H_2S induced by H_2O_2

RAW 264.7 cells were suspended and then seeded into a 6-cell plate at a density of 40 000 cells per well. The cells were cultured until they reached 80% confluency. After the medium was removed, the confluent cells were washed with PBS, and then FBS-free DMEM containing PTCM (50 μM) and 7-azido-4-methylcoumarin (AzMC, 5 μM, Sigma, USA) was added and the cells were incubated for 30 min. The extracellular AzMC and PTCM were washed with PBS and incubated with FBS-free DMEM containing different concentrations of H_2O_2 (0, 25 μM, and 50 μM) for 30 min. H_2O_2 and suspended cells were removed by washing with PBS, and the cells were observed with an IX71 inverted fluorescence microscope (Olympus, Japan) under excitation with a 365 nm laser.

2.11. Cell immunofluorescence

RAW 264.7 cells were seeded in 6-well plates (1×10^6 cells per well) and incubated for 24 h in an incubator. After confluent cells were removed with PBS, the media containing H_2O_2 (50 μM) and PTCM@PMet NPs (50 μM) were added, respectively, and incubated for 24 h. The medium was removed and washed with PBS. 4% paraformaldehyde was added to fix the cell for 15 min at r.t. and maintained in 0.5% (v/v) Triton X-100 (Beyotime, ST677, China) in PBS for 5 min. 1% (w/v) bovine serum albumin (BSA, Beyotime, ST025, China) in PBS was utilized as a blocking agent for 30 min. Subsequently, the cells were treated with CD206 1% (w/v) BSA for 30 min at 4 °C. After washing with PBS, the cells were incubated with goat anti-rabbit IgG(H + L) CoraLite (1 : 100, SA00013-4, Proteintech, China) secondary antibodies for 1 h at 37 °C in the absence of light. Following this, the cells were cultured with a DAPI working solution (10 μg mL^{-1}, C0065, Solarbio, China) at r.t. for 10 min in the absence of light. Finally, the fluorescence images were observed using a Nikon Eclipse-Ti laser scanning confocal microscope (LSCM, NIKON, Japan).

2.12. Migration assay

HUVECs were seeded in 6-well plates (1×10^6 cells per well). When the cells reached 80–90% confluency, a 200 μL sterile pipette tip was used to draw a straight scratch across the cells, and the dropped cells were washed with PBS. The cells were incubated with PTCM@PMet NPs (50 μM) + H_2O_2 (50 μM) to study the effect of H_2S on cell migration. The scratch healing was observed using an IX71 inverted fluorescence microscope at 0, 12, and 24 h time points and the healing ratio of the scratch area was quantified using ImageJ 1.8 software.

2.13. Transwell assay

After the addition of PTCM@PMet NPs (50 μM), H_2O_2 (50 μM), and 600 μL complete medium to the lower section of 6.5 mm transwell chambers with 8 μm pores (3422, Corning), HUVECs in the logarithmic growth phase cultured in serum-free medium for 12 h were seeded on the upper section of the cell compartment and incubated for 24 h. The medium of the upper section of cell chambers was removed and the cells were softly cleaned with a cotton swab. The cell was fixed with 4% paraformaldehyde for 30 min after two washes with pre-cooled PBS. Then moderate air drying was used, and the cells were stained with 0.1% crystal violet (G1063, Solarbio, China) for 20 min. After being washed three times with pre-cooled PBS, the migratory cells that had attached to the lower surface of the chamber were observed using an IX71 inverted fluorescence microscope.

2.14. Tube formation

Matrigel (356234, Corning, USA) was added to pre-chilled 24-well plates (100 μL per well) and incubated in a 37 °C incubator for 30 min. HUVECs (20 000 cells per well) were seeded into the plates. After 6 h of culture in the incubator, the tube network was observed with an IX71 inverted fluorescence microscope. The number of tube branches was quantified using ImageJ 1.8 software.

2.15. Detection of intracellular ROS production

Intracellular ROS production was assessed using a DCFH-DA assay kit (S0033S, Beyotime, China). RSCs were seeded in 12-well plates and respectively cultured with DMEM containing

H_2O_2 (50 μM) and PTCM@PMet NPs (50 μM) for 24 h. After washing with PBS, H_2O_2 (400 μM) was added into the plate. After 12 h of incubation, the cells were cultured in FBS-free DMEM containing DCFH-DA (10 μM) for 45 min in an incubator. The intracellular ROS production was observed using an IX71 inverted fluorescence microscope.

2.16. Detection of mitochondrial membrane potential

JC-1 (M8650, Solarbio, China) was used to evaluate the mitochondrial membrane potential. HUVECs were seeded in 12-well plates and respectively cultured with F-12K medium containing H_2O_2 (50 μM) and PTCM@PMet NPs (50 μM) for 24 h. The intracellular materials and suspended cells were washed with PBS, then H_2O_2 (400 μM) was added into the plate and cultured for 12 h. JC-1 staining working solution was added into the plate and cultured for 20 min in an incubator. After washing twice with JC-1 staining buffer, 1 mL F12K medium was added into the well and observed with an IX71 inverted fluorescence microscope.

2.17. Hematoxylin and eosin staining

The sections at 5 and 14 days were first soaked in xylene to remove the wax, followed by rehydration in a series of decreasing alcohol concentrations (100%, 90%, and 80%) and water. The sections were stained with hematoxylin for 5 min, washed with PBS, stained with eosin for 2 min, and washed with water. The sections were dehydrated in increasing alcohol concentrations (80%, 90%, and 100%) and then cleared in xylene. The stained sections were mounted with neutral resin and observed with a microscope.

2.18. Masson's trichrome staining

Sections at 14 days were deparaffinized and rehydrated. Sections were stained with iron hematoxylin and washed with water and acid alcohol for differentiation. Subsequently, the sections were sequentially treated with ponceau acid fuchsin solution, 2% acetic acid solution, phosphomolybdic acid solution, and aniline blue. As previously stated, the sections underwent dehydration, mounting, and cover-slipping. The image collection and analysis were performed using a microscope and ImageJ 1.8 software.

2.19. Immunofluorescence staining

Sections were deparaffinized and rehydrated. A solution containing 3% H_2O_2 was employed to eliminate the endogenous peroxidase activity, while 5% BSA was utilized to prevent nonspecific binding of the sections. Sections of 5, 7, and 14 days were immune-stained with CD86 (1 : 200, rabbit polyclonal antibody, bs-1035R, Bioss, China), CD163 (1 : 500, rabbit polyclonal antibody, ab182422, abcam, China), CD31 (1 : 200, rabbit polyclonal antibody, GB113151, Servicebio, China), GAP-43 (1 : 2000, rabbit polyclonal antibody, GB11095, Servicebio, China), and S100 (1 : 200, rabbit polyclonal antibody, GB1139, Servicebio, China). After being washed with PBS, the sections were incubated with the following secondary antibodies: BHR-labeled goat anti-rabbit IgG (H + L) (1 : 400, 5220-0336, SeraCare, China), BHR-labeled goat anti-rabbit IgG (H + L) (1 : 500, GB23204, Servicebio, China), Alexa Fluor 594-labeled goat anti-rabbit IgG (1 : 400, 111-585-003, Jackson, USA), Cy3-labeled goat anti-rabbit IgG (H + L) (1 : 300, GB21303, Servicebio, China), and Alexa Fluor 488-labeled goat anti-rabbit IgG (H + L) (1 : 400, GB25303, Servicebio, China). The incubation period lasted for 50 min at r.t. in the dark. The section was counterstained with DAPI, and the resulting fluorescent images were visualized using a Nikon Eclipse C1 confocal laser microscope (Nikon, Tokyo, Japan). The ImageJ 1.8 software was utilized for quantitative analysis of each image.

2.20. Data analysis

All data are presented as mean ± standard deviation (SD). Statistical analysis for multiple comparisons was conducted using one-way analysis of variance (ANOVA) followed by Tukey's post hoc test. Statistical analysis and data visualization were performed using GraphPad Prism 9 software (GraphPad Software Inc., La Jolla, CA, USA).

2.21. Ethics statement

All animal studies were carried out in compliance with the regulations and guidelines of the Wuhan University of Technology and conducted according to the Institutional Animal Care and Use Committee (IACUC) guidelines.

3. Results and discussion

3.1. Synthesis and physiochemical characterization of PTCM and F127-P(Asp-NHS)

The synthesis of PTCM and the responsive release mechanism of H_2S are depicted in Fig. 2A. Firstly, the phenylboronic acid pinacol ester of PTCM is oxidized to phenolic hydroxyl groups in the presence of hydrogen peroxide (H_2O_2). Subsequently, it underwent a 1,6-elimination reaction, resulting in the formation of 4-fluoroaniline, 4-hydroxybenzyl alcohol, and carbonyl sulfide (COS). Finally, under the catalytic action of carbonic anhydrase (CA), COS was hydrolyzed to produce H_2S. The characterization results from ^{1}H nuclear magnetic resonance (^{1}H NMR) spectroscopy and high resolution mass spectrometry (HRMS) are shown in Fig. S1 and S2 (ESI†). The reduction peak of the benzyl proton of PTCM at 5.5 ppm or 4-hydroxy benzyl at 4.4 ppm could be used to calculate the release rate of COS from PTCM in the presence of H_2O_2 (Fig. 2B), which achieved 86.60% in 24 h, indicating the extreme sensitivity of PTCM to ROS.

PTCM could be easily encapsulated into nanoparticles by self-assembly of amphiphilic poly(amino acid) mPEG-PMet, which could be synthesized by the ring-opening polymerization of L-methionine *N*-carboxy anhydride (Met NCA) initiated by mPEG-NH_2 (M_n = 4000) (Fig. 2C). Due to the susceptibility of the thioether group in the side chain of methionine (Met) to oxidation, when exposed to a microenvironment of oxidative stress, it could undergo conversion to hydrophilic sulfoxide or sulfone, leading to a phase transition (Fig. 2D). The ^{1}H NMR characterization results of the synthesis of mPEG-PMet are

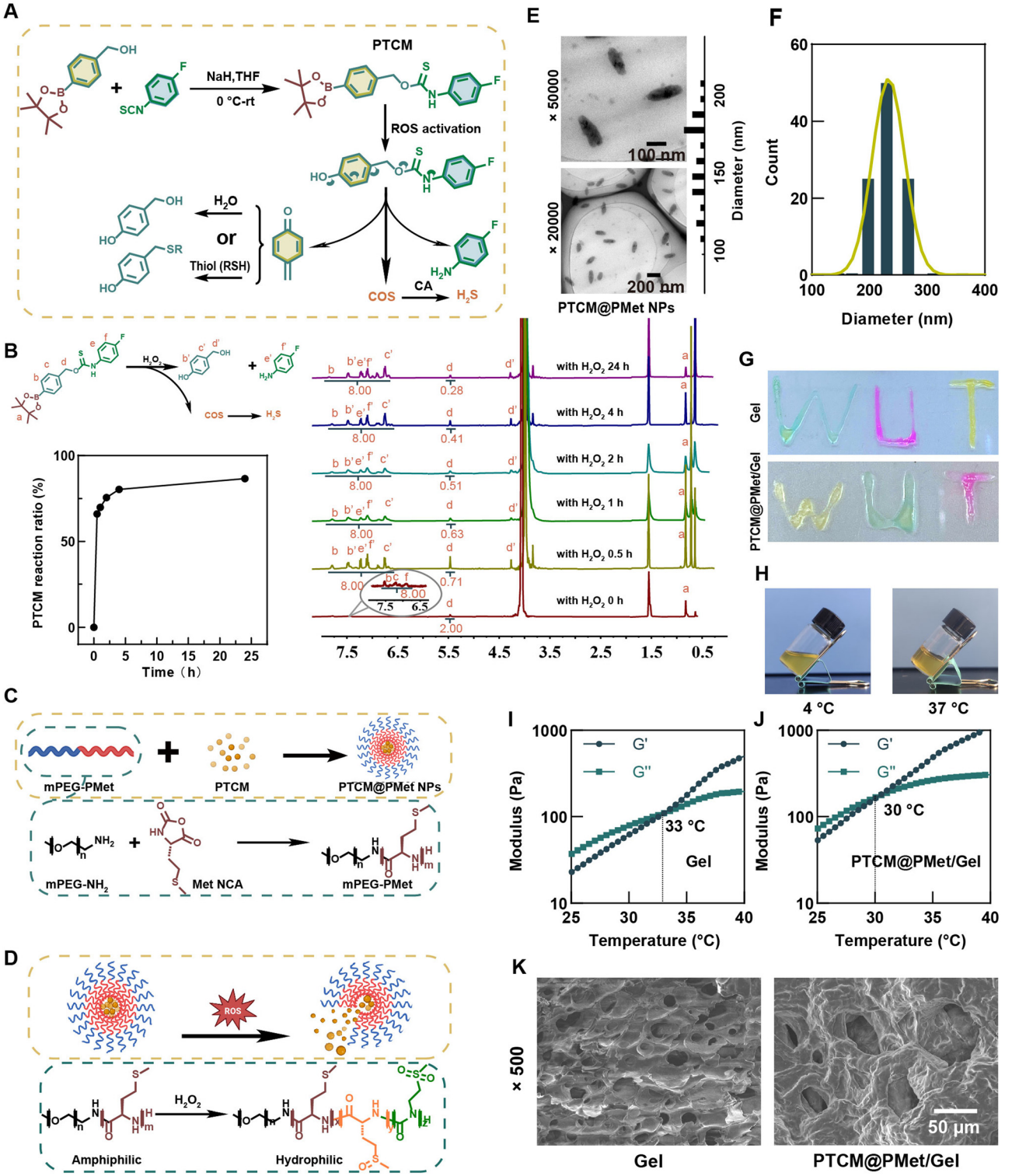

Fig. 2 Synthesis and physicochemical characterization of H_2S scalded wound dressing. (A) Synthesis of PTCM and release mechanism of H_2S in response to ROS. (B) ^1H NMR study of H_2O_2-induced decomposition of PTCM. (C) Schematic illustration of PMet and co-assembly with PTCM into NPs. (D) Schematic diagram and mechanism of drug release from PTCM@PMet NPs with activation by ROS. (E) TEM images and size distributions of PTCM@PMet NPs. (F) Particle size distributions of PTCM@PMet NPs measured by DLS. (G) The injectability of F127-P(Asp-NHS) and PTCM@PMet/F127-P(Asp-NHS) hydrogels. (H) Photographs of the hydrogel at different temperatures. (I) and (J) Rotational rheological properties of F127-P(Asp-NHS) and PTCM@PMet/F127-P(Asp-NHS) hydrogels (storage modulus G' and loss modulus G''). (K) SEM images of F127-P(Asp-NHS) and PTCM@PMet/F127-P(Asp-NHS) hydrogels.

presented in Fig. S4 (ESI†). Transmission electron microscopy (TEM) was employed to observe the uniform rod-like structure of PTCM@PMet NPs (Fig. 2E). Additionally, the average particle size of the NPs was measured to be 229.8 nm using dynamic light scattering (DLS) (Fig. 2F).

To explore the ROS responsive ability of PTCM@PMet NPs, they were incubated with H_2O_2 (50 μM) and the cumulative release of PTCM was detected. With the increase of H_2O_2 concentration, the release of PTCM also increased significantly (Fig. S5, ESI†). When stimulated with 50 μM H_2O_2, about 23.37% of PTCM was released from the nanoparticles at 48 h, while only 6.22% was released from the pure PBS group.

The amphiphilic poly(amino acid) F127-P(Asp-NHS) was synthesized through the ring-opening polymerization of Asp *N*-carboxy anhydride (Asp NCA), with initiation by F127-NH_2 (M_n = 12 600). The results of the ^{1}H NMR characterization are also presented in Fig. S6 (ESI†). The F127-P(Asp-NHS) compound could be injected through a syringe to inscribe the word "WUT" (Fig. 2G) and then underwent a phase transition to form a hydrogel at a temperature of 37 °C, as depicted in Fig. 2H. The rheological characteristics showed that the F127-P(Asp-NHS) hydrogel (Gel) exhibited unique thermosensitivity, and with the addition of PTCM@PMet NPs, the critical sol–gel transition temperature decreased from 33 °C to 30 °C (Fig. 2I and J).

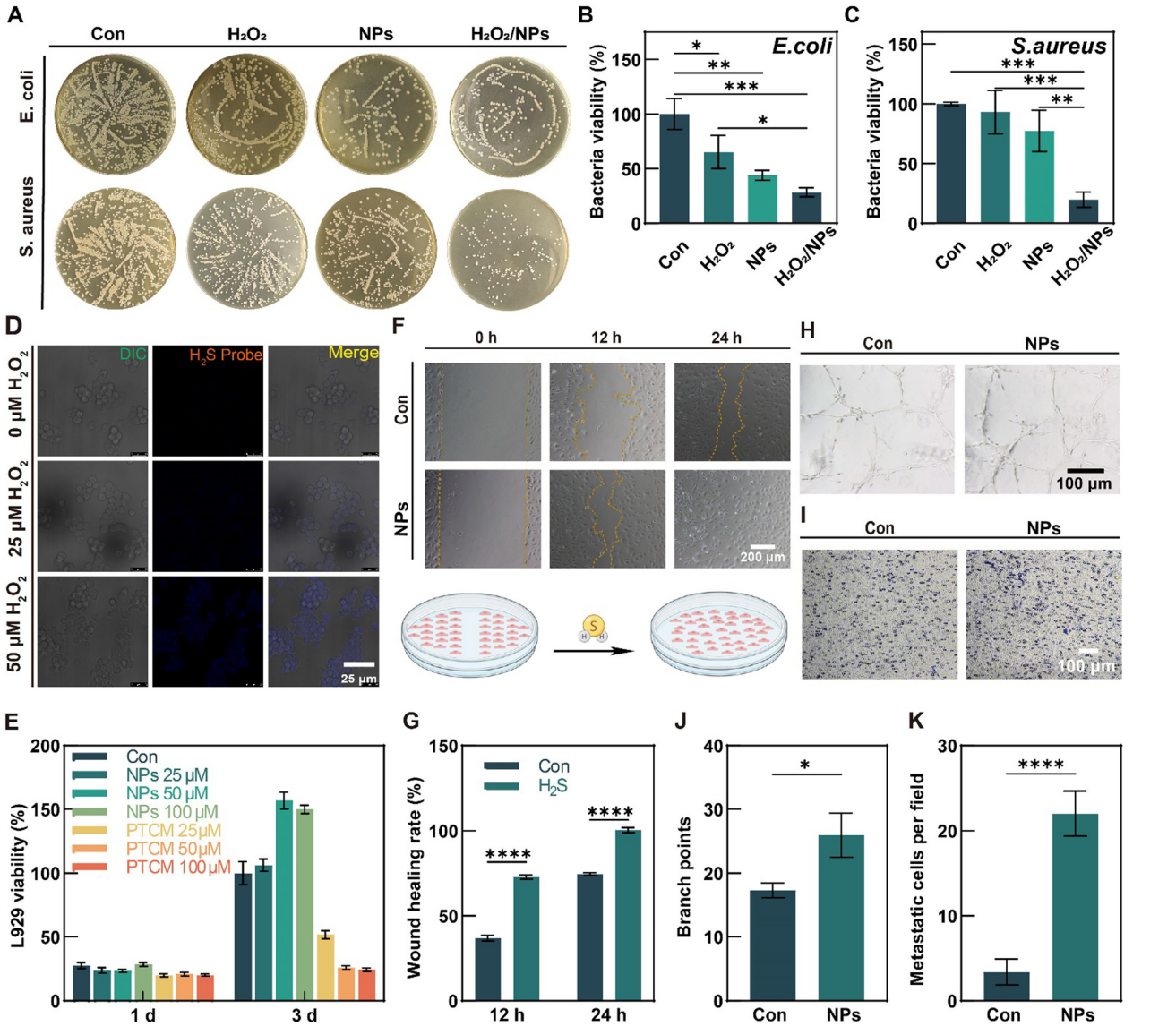

Fig. 3 *In vitro* antibacterial performance, cytocompatibility, and angiogenesis of PTCM@PMet NPs. (A) Images in the antibacterial performance test against *E. coli* and *S. aureus*. (B) and (C) Quantitative analysis of bacterial viability. (D) The cellular uptake of PTCM with RAW264.7 and release of H_2S with the activation of H_2O_2 at 3 days. (E) L929 viability after being cultured with PTCM@PMet NPs for 1 and 3 days to assess the cytocompatibility. (F) Scratch tests assessing the effect of H_2S on HUVECs migration at different times (0, 12, and 24 h). (G) Statistical results of the scratch wound healing rate. (H) HUVEC tube formation assessing the effect of H_2S on angiogenesis at 6 h. (I) The effect of H_2S on HUVEC migration tested by the transwell method. Statistical results of (J) branch point of the formative tube and (K) HUVEC migration. *$p < 0.05$, **$p < 0.01$, ***$p < 0.001$, ****$p < 0.0001$.

Frequency–storage modulus (G') (0.01–100 Hz, 1% strain) curves showed that the G' of the hydrogel was frequency-dependent within a certain frequency range (0–31 Hz), possibly because the motion of the polymer chain is unable to keep up with the change in frequency, resulting in an increase in the modulus (Fig. S7A, ESI†). Strain sweep (0.01–1000% strain, 10 Hz) results indicated that the addition of PTCM@PMet NPs significantly enhanced the storage modulus of the hydrogel (Fig. S7B, ESI†). We speculate that the interaction between the amino groups of the PTCM@PMet NPs and the F127-P(Asp-NHS) matrix increased the crosslinking density and strengthened the hydrogel. SEM images of F127-P(Asp-NHS) and PTCM@PMet/F127-P(Asp-NHS) (PTCM@PMet/Gel) revealed the presence of a sheet-like structure with micrometer-sized pores (Fig. 2K). The porous structure of the hydrogel could facilitate cell growth and maintain a moist environment for wound healing.

3.2. *In vitro* antibacterial activity of PTCM@PMet NPs

Scalds are frequently accompanied by massive exudation of body fluids, rendering the wound susceptible to infection.[50] Therefore, in the design of a scald wound dressing, it is imperative to select a material that possesses an antibacterial effect in order to effectively prevent the occurrence of infection.[2] We employed *Escherichia coli* (a Gram-negative bacterium) and *Staphylococcus aureus* (a Gram-positive bacterium) as representative bacterial strains to assess the antibacterial efficacy of PTCM@PMet NPs (NPs) (Fig. 3A). According to Fig. 3B and C, the H_2O_2/NPs group exhibited a 71.58% inhibition rate against *E. coli* and an 80.23% inhibition rate against *S. aureus*, when compared to the control group (Con). The findings of this study suggested that H_2S possesses antibacterial properties, thereby potentially serving as a preventive measure against infection.

3.3. *In vitro* release of H_2S from PTCM

As a fluorescent probe,7-azido-4-methylcoumarin (AzMC) can be reduced by H_2S to generate 7-amino-4-methylcoumarin (AMC) with fluorescence, which can be used to monitor the accumulation of H_2S in the cells. Representative fluorescence images are shown in Fig. 3D. The results indicated that AMC fluorescence was not detected in the control group without H_2O_2, and PTCM did not release H_2S in a typical cellular environment. By contrast, the AMC fluorescence was observed in mouse mononuclear macrophage cells (RAW264.7) with H_2O_2, and it increased with the concentration increase of H_2O_2 from 25 μM to 50 μM, indicating that ROS can activate PTCM to release H_2S in the cellular environment.

3.4. Cytocompatibility evaluation of PTCM@PMet NPs

As potential therapeutic agents for scalded wound management, PTCM@PMet NPs should be noncytotoxic. L-mouse fibroblast cells (L929) were used to evaluate the cytocompatibility of PTCM@PMet NPs by the CCK-8 assay. The results indicated that there was no significant difference between the control group and the NPs group after 1 and 3 days of culture (Fig. 3E). This result indicated that 50 μM PTCM alone had a significant cytotoxicity, but the cytotoxicity was reduced by PMet encapsulation. Therefore, 50 μM effective drug concentration was selected as the experimental concentration in this paper.

3.5. H_2S stimulates cell angiogenesis

As HUVECs are frequently employed to evaluate cell angiogenesis *in vitro*,[51] PTCM@PMet NPs were incubated with HUVECs to study the effect of H_2S on HUVEC migration and tube formation. Scratch closure was observed at 12 h and 24 h after incubation. As shown in Fig. 3F, the PTCM@PMet NPs group showed better cell migration, with smaller scratches after 12 h than the control (Con) group and almost closed scratches after 24 h, and the statistical analysis results also showed that H_2S promoted cell migration (Fig. 3G). The tube formation is another important indicator to evaluate angiogenesis.[52] Representative images depicting the tube formation of HUVECs in the control and PTCM@PMet NPs groups after 6 h of *in vitro* incubation are presented in Fig. 3H. Following 6 h of culture, the PTCM@PMet NPs group exhibited a more pronounced tube network and the statistical analysis of the tube branch numbers revealed significantly more branches compared to the control group (approximately 1.5 times higher) (Fig. 3J). The effect of H_2S released in the culture medium on the migration of HUVECs was further investigated using the transwell method (Fig. 3I). The statistical results showed that the migration of HUVECs of the NPs group was significantly enhanced compared to the control group (Fig. 3K). The findings suggested that PTCM@PMet NPs could achieve high temporal and spatial release of H_2S and thus could be used for the precise management of the microenvironment in injury sites.

3.6. H_2S reduces oxidative stress

Nerves play a crucial role in the regulation of inflammation, angiogenesis, granulation hyperplasia, and post-healing remodeling during the process of wound healing.[53–55] Oxidative stress resulting from inflammation and ischemia in scalded wounds can induce neuronal apoptosis, impede nerve regeneration, complicate wound healing, and hinder functional recovery of the skin.[56,57] Therefore, the appropriate regulation of wound redox homeostasis to establish a microenvironment is favorable for nerve regeneration and facilitates the process of wound healing. In order to examine the potential protective effects of H_2S on the mitochondrial function of RSCs against oxidative stress-induced damage, RSCs were subjected to H_2O_2 treatment for 24 h to establish an oxidative stress model. Subsequently, these cells were incubated with PTCM@PMet NPs (NPs), and the DCFH-DA assay was employed to measure the intracellular ROS levels following the treatment of H_2O_2-pretreated RSCs with PTCM@PMet NPs (Fig. 4A). The results demonstrated a significant increase in intracellular ROS levels in RSCs following H_2O_2 incubation. Conversely, the H_2O_2/NPs group was found to reduce ROS production (Fig. 4D). Stable mitochondrial membrane potential (MMP) is beneficial for maintaining normal cellular physiological functions, and it is also a prerequisite for maintaining mitochondrial oxidative phosphorylation and ATP generation.[58] JC-1 was used to study

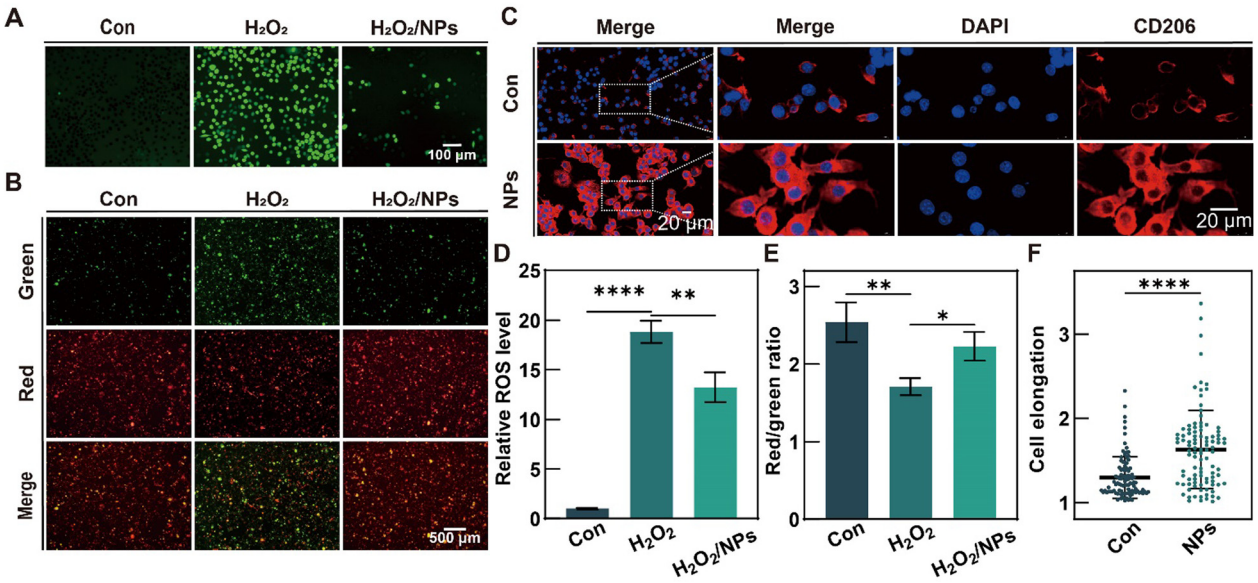

Fig. 4 *In vitro* antioxidant and anti-inflammatory effects of H_2S. (A) Fluorescent images of ROS in RSCs using DCFH-DA (fluorescent probe). (B) Mitochondrial membrane potential of RSCs detected with JC-1 fluorescent staining (red fluorescence: high MMP; green fluorescence: low MMP). (C) Representative images of CD206 immunofluorescence staining of RAW 264.7 treatment with PTCM@PMet NPs (effective drug concentration: 50 μM). (D) Statistical results of relative ROS levels, (E) ratio of red to green fluorescence of JC-1, and (F) elongation rate of macrophages. *$p < 0.05$, **$p < 0.01$, ***$p < 0.001$, ****$p < 0.0001$.

the alleviation of H_2O_2-induced mitochondrial damage by H_2S (Fig. 4B and E). The results showed that H_2O_2 treatment significantly reduced the MMP of RSCs, while the presence of PTCM@PMet NPs alleviated the decrease in MMP caused by H_2O_2. These results demonstrated that H_2S possessed a significant antioxidant capacity and could reconstruct redox homeostasis.

3.7. Anti-inflammatory effects of H_2S by inducing macrophage polarization

RAW264.7 was employed to assess the potential of H_2S in inducing phenotypic alterations that may result in anti- or pro-inflammatory effects. PTCM@PMet NPs was incubated with RAW264.7, and after 3 days, macrophage morphology was observed with immunofluorescence staining for the M2 macrophage surface marker (CD206) (Fig. 4C). The results indicated that the control group showed round macrophages, while the cells in the NPs group showed slender macrophages with 1.26 times greater cell elongation than those in the control (Con) group (Fig. 4F). Specifically, the process of macrophage polarization towards the M2 phenotype is strongly associated with cellular elongation.[59] The fluorescence intensity of CD206 on the surface of macrophages treated with PTCM@PMet NPs was significantly increased, indicating that the polarization of macrophages to M2 phenotype could be induced by H_2S.

3.8. H_2S facilitates the healing process of scalded wounds

The *in vivo* efficacy of H_2S in promoting scalded wound healing was investigated using a scald model on Sprague–Dawley (SD) rats (Fig. 5A). Firstly, two days after the scald treatment, a 15 mm diameter punch was used to construct a full-thickness wound, resulting in an actual wound diameter of 20 mm due to skin relaxation. Then, rats with full-thickness scalded wounds were randomly divided into three groups: the control (Con) group, the F127-P(Asp-NHS) hydrogel (Gel) group, and the PTCM@PMet NPs/F127-P(Asp-NHS) hydrogel (H_2S/Gel) group. The control group received treatment with normal saline, while the experimental groups were administered precursor solutions of the materials directly into the wound in the dorsal region of mice to induce *in situ* gelation by body temperature. The healing progress of all groups was assessed on days 0, 5, 10, 14, and 28 (Fig. 5B). On the fifth day, the wound area of the H_2S/Gel group was found to be only 31.00%, in contrast to the 50.04% observed in the Con group and the 54.43% observed in the Gel group (Fig. 5E). Over the course of time, the wounds sustained by each group gradually healed to smaller wounds, and the wound area was measured. It was observed that the wound area of the Con group and the Gel group exhibited a significantly higher level compared to the H_2S/Gel group. After a treatment period of 28 days, the wound area in the Con group and the Gel group was reduced to 13.23% and 12.71%, respectively, whereas the H_2S/Gel group was only 4.57%. At 14 days, the Con group and the Gel group were still at the end of the inflammatory phase, with blood scab, while the H_2S/Gel group had entered the proliferative phase. At 28 days, there were only tiny scars in the experimental group, while the scars in the Con group and the Gel group were more obvious. These results indicated that H_2S-releasing dressing could promote the healing process of scalded wounds.

As typical indicators to evaluate the wound healing process, the wound re-epithelialization and granulation tissue formation were analyzed by hematoxylin and eosin (H&E) staining

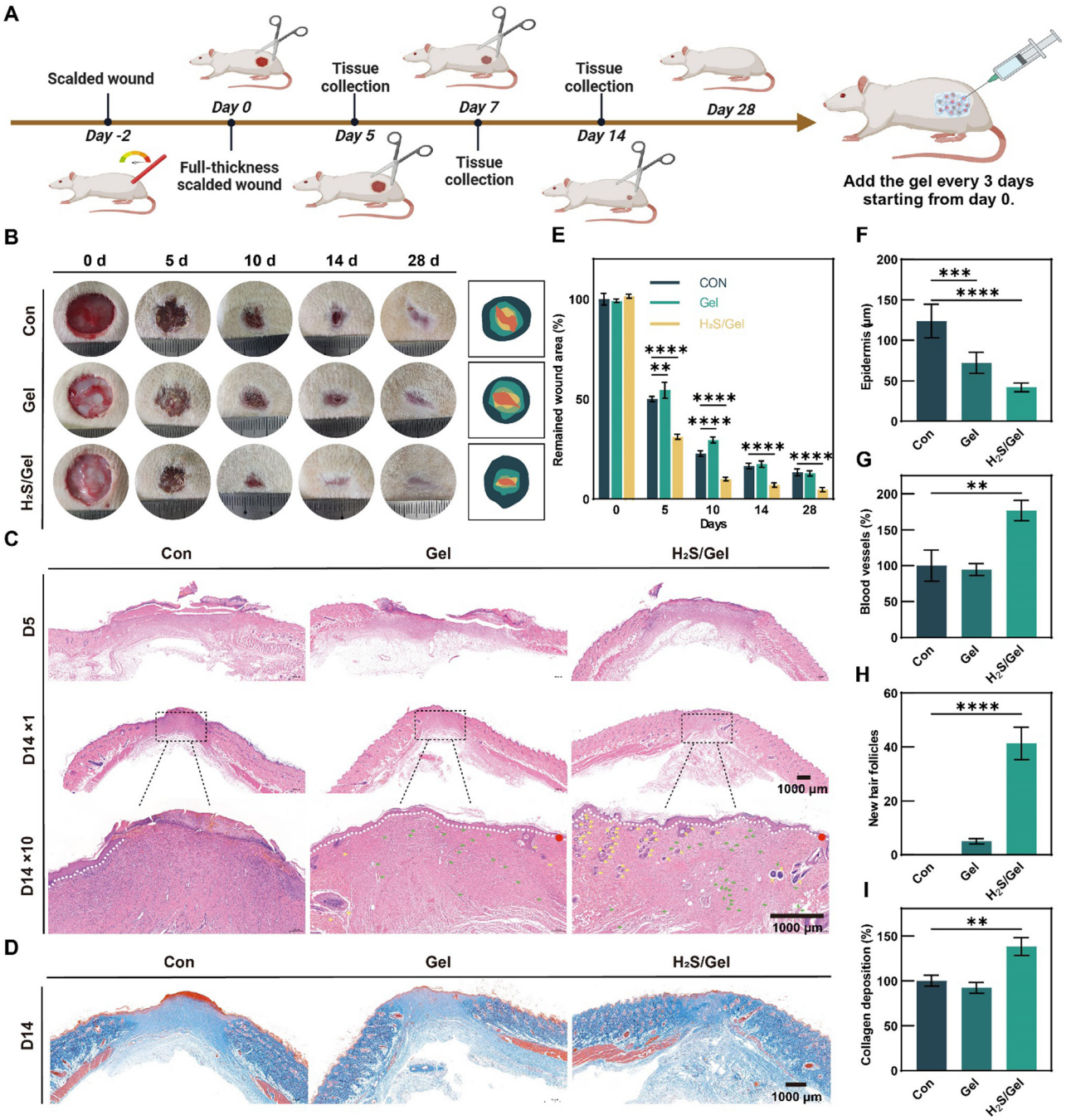

Fig. 5 PTCM@PMet NPs/F127-P(Asp-NHS) hydrogel promoted scalded wound healing *in vivo via* constructing a regenerative microenvironment. (A) Schematic diagram illustrating the timeline of the operation process. (B) The representative images and schematic presentation of the wound healing. (C) Images of H&E staining of regenerative skin in the three groups on the 5th and 14th days (white dashed line: the boundary of the epithelium and dermis; yellow arrow: hair follicles; green arrow: blood vessels; red dot: complete epithelium). (D) Images of Masson's trichrome staining on day 14. (E) *In vivo* wound closure rates at different time points of the three groups. (F) Epidermis thickness of different groups on the 14th day. (G) The regenerated blood vessels on the 14th day. (H) Hair follicle numbers of different groups on the 14th day. (I) The collagen deposition of different groups on the 14th day. $*p < 0.05$, $**p < 0.01$, $***p < 0.001$, $****p < 0.0001$.

(Fig. 5C).[60,61] At day 5 of treatment, the epidermal and dermal structures of each group showed obvious defects, and the wound has contracted. Compared with the Con and Gel groups, the H_2S/Gel group showed significantly less inflammatory infiltration and a small amount of granulation tissue and neovascularization, which was due to the accelerated healing process induced by the anti-inflammatory and antibacterial properties of H_2S.[62] After 14 days of treatment, some new epithelial tissue was formed in both H_2S/Gel and Gel groups, but the epithelial thickness was thinner in the H_2S group,

indicating that mature epithelial structure was reconstructed faster, while there was still persistent scab in the Con group, indicating incomplete re-epithelialization and delayed healing processes (Fig. 5F). In addition, the H_2S/Gel group exhibited a higher number of newly formed vascular and hair follicles compared to the other groups (Fig. 5G and H). This observation suggests that the H_2S-releasing dressing initiated the function reconstruction of skin, which can be attributed to the multiple effects exerted by H_2S during wound healing.

Masson's trichrome staining on regenerated skin sections was performed at the 14th day to analyze the formation and composition of collagen fibers in the regenerated skin.[51] According to Fig. 5D, the collagen fibers in the Con group and the Gel group exhibited sparse and disordered staining, with a small number of fibers observed. In contrast, the collagen fibers in the H_2S/Gel group were evenly and neatly distributed. Through statistical analysis, it was observed that the deposition of collagen fibers in the H_2S/Gel group was significantly greater compared to the other two groups (Fig. 5I).

To examine the potential ability of H_2S during the initial inflammatory phase of wound healing, the immunostaining for CD86 (surface marker of M1) and CD163 (surface marker of M2) was conducted on the 5th day (Fig. 6A and B). Fluorescence images revealed that, in comparison to the Con group and the Gel group, the H_2S/Gel group exhibited a down-regulation in

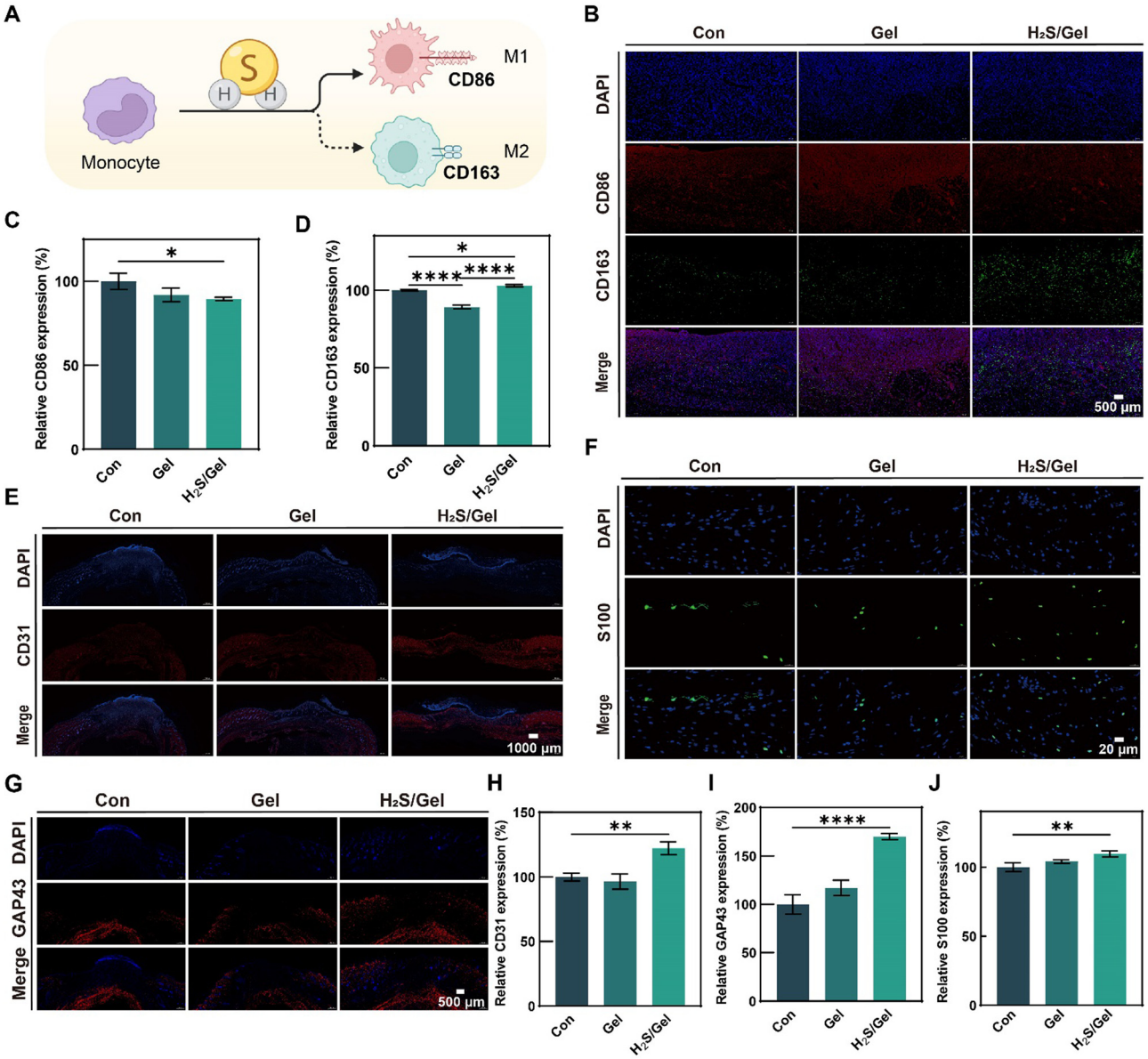

Fig. 6 H_2S induces macrophage polarization, revascularization, and nerve regeneration *in vivo*. (A) Schematic representation of macrophage polarization induced by H_2S. (B) DAPI/CD86/CD163 immunofluorescent staining of regenerative skin on the 5th day. Statistical results of (C) CD86 and (D) CD163. (E) DAPI/CD31 immunofluorescent staining of regenerative skin on the 7th day. (F) DAPI/S100 immunofluorescent staining of regenerative skin on the 14th day. (G) DAPI/GAP43 immunofluorescent staining of regenerative skin on the 14th day. Statistical results of (H) CD31, (I) GAP43, and (J) S100. *$p < 0.05$, **$p < 0.01$, ***$p < 0.001$, ****$p < 0.0001$.

the expression level of CD86 and an up-regulation in the level of CD163 (Fig. 6C and D). The results presented in this study demonstrated that H_2S had the ability to facilitate the polarization of macrophages toward the M2 phenotype, thereby reducing inflammation in the wound.

As an important role in the process of skin regeneration, blood vessels enable the transport of nutrients and growth factors.[63] Therefore, the vascular marker CD31 of the regenerated tissue was analyzed by immunostaining on the 7th day. The wound section from the H_2S/Gel group had more CD31 expression compared to the Con group and Gel group (Fig. 6E). Quantitative analysis showed that the relative coverage of CD31 in the H_2S/Gel group was 9% and 5% higher in the Con and Gel groups (Fig. 6H). The results showed that the introduction of H_2S could effectively enhance the revascularization.

In the process of scalded wound repair, nerves can effectively regulate the function of cells and affect skin regeneration and functional recovery.[64] Immunostaining analyses of the underlying neuropathy maker S100 and the skin characteristic neural marker GAP43 were performed on the regenerated tissue at day 14 to assess nerve regeneration (Fig. 6F and G). The results demonstrated that the H_2S/Gel group exhibited a significant increase in the expression of S100 and GAP43 compared to the Con and Gel groups (Fig. 6I and J). These findings suggested that H_2S played a role in promoting nerve regeneration. These *in vivo* observations and evaluations provided compelling evidence that the utilization of H_2S scald dressing had a significant positive impact on the overall healing process, thereby promoting the healing of scalded wounds.

4. Conclusion

In conclusion, considering the challenges associated with the healing process of scalded wounds, such as infection, oxidative stress, persistent inflammation, and the difficulties of vascular and neural regeneration, this study has developed an H_2S "intelligent warehouse" scald dressing using an F127-P(Asp-NHS) hydrogel and PTCM@PMet NPs. The aim of this dressing is to synergistically promote the repair of scalded wounds. As a responsive drug-loaded NP system, the scalded microenvironment marker ROS was used as the excitation source of PTCM@PMet NPs. At the scald site, H_2S can adaptively be released according to the level of ROS, which can effectively and dynamically regulate the inflammatory and oxidative stress of the wound microenvironment, inhibit the growth of bacteria, promote the regeneration of nerves and blood vessels, improve tissue remodeling, and accelerate the wound healing and functional recovery of skin. The research results help to explore the feasibility of gas signaling molecules for scalded wound repair and provide a new scheme to solve the problems of slow wound healing caused by long-term inflammation and oxidative stress.

Author contributions

Junwei Yang: conceptualization, methodology, formal analysis, investigation, methodology, writing – original draft. Xianzhen Dong: conceptualization, methodology, data curation. Wenying Wei: conceptualization, writing – review, data curation. Kun Liu: methodology, writing – review. Xiaopei Wu: funding acquisition, project administration. Honglian Dai: conceptualization, resources, supervision, writing – review and editing, project administration.

Conflicts of interest

There are no conflicts to declare.

Acknowledgements

This work was supported by grants from the National Natural Science Foundation of China (52372272, 32201109, and 32360234), the Guangdong Basic and Applied Basic Research Foundation (2022B1515120052 and 2021A1515110557), the Key Basic Research Program of Shenzhen (JCYJ20200109150218836), and the Self-innovation Research Funding Project of Hanjiang Laboratory (HJL202202A002).

References

1 Y. Dong, M. Cui, J. Qu, X. Wang, S. H. Kwon, J. Barrera, N. Elvassore and G. C. Gurtner, *Acta Biomater.*, 2020, **108**, 56–66.
2 Y. Yao, A. Zhang, C. Yuan, X. Chen and Y. Liu, *Biomater. Sci.*, 2021, **9**, 4523–4540.
3 A. E. Stoica, C. Chircov and A. M. Grumezescu, *Materials*, 2020, **13**, 2853.
4 L. DeSanti, *Adv. Skin Wound Care*, 2005, **18**, 323–332; quiz 332–324.
5 S. A. Eming, M. Hammerschmidt, T. Krieg and A. Roers, *Semin. Cell Dev. Biol.*, 2009, **20**, 517–527.
6 J. Wu, A. Chen, Y. Zhou, S. Zheng, Y. Yang, Y. An, K. Xu, H. He, J. Kang, J. A. Luckanagul, M. Xian, J. Xiao and Q. Wang, *Biomaterials*, 2019, **222**, 119398.
7 L. Xi, L. Wang, M. Zhang, C. He, X. Yang, Y. Pang, H. Chen and F. Cheng, *ACS Biomater. Sci. Eng.*, 2023, **9**, 5843–5854.
8 J. C. Harris, M. A. Scully and E. S. Day, *Cancers*, 2019, **11**, 1836.
9 B. Hoesel and J. A. Schmid, *Mol. Cancer*, 2013, **12**, 86.
10 M. G. Jeschke, D. L. Chinkes, C. C. Finnerty, G. Kulp, O. E. Suman, W. B. Norbury, L. K. Branski, G. G. Gauglitz, R. P. Mlcak and D. N. Herndon, *Ann. Surg.*, 2008, **248**, 387–400.
11 L. Miao, X. Y. Shen, M. Whiteman, H. Xin, Y. Q. Shen, X. M. Xin, P. K. Moore and Y. Z. Zhu, *Antioxid. Redox Signalling*, 2016, **25**, 268–281.
12 F. Y. McWhorter, T. T. Wang, P. Nguyen, T. Chung and W. F. Liu, *Proc. Natl. Acad. Sci. U. S. A.*, 2013, **110**, 17253–17258.
13 F. Y. McWhorter, C. T. Davis and W. F. Liu, *Cell. Mol. Life Sci.*, 2015, **72**, 1303–1316.

14 L. Teng, Y. Song, L. Hu, Q. Bai, X. Zhang and C. M. Dong, *Chin. J. Chem.*, 2023, **41**, 2103–2112.
15 H. Yan, J. Du, S. Zhu, G. Nie, H. Zhang, Z. Gu and Y. Zhao, *Small*, 2019, **15**, 1904382.
16 L. R. Goodwin, D. Francom, F. P. Dieken, J. D. Taylor, M. W. Warenycia, R. J. Reiffenstein and G. Dowling, *J. Anal. Toxicol.*, 1989, **13**, 105–109.
17 F. Rong, T. Wang, Q. Zhou, H. Peng, J. Yang, Q. Fan and P. Li, *Bioact. Mater.*, 2023, **19**, 198–216.
18 Y. X. Ge, F. Rong, W. Li and Y. Wang, *J. Controlled Release*, 2022, **352**, 586–599.
19 H.-J. Sun, Z.-Y. Wu, X.-W. Nie, X.-Y. Wang and J.-S. Bian, *J. Adv. Res.*, 2021, **27**, 127–135.
20 M. Xu, L. Zhang, S. Song, L. Pan, I. Muhammad Arslan, Y. Chen and S. Yang, *J. Adv. Res.*, 2021, **27**, 11–17.
21 Y. Zhao, T. D. Biggs and M. Xian, *Chem. Commun.*, 2014, **50**, 11788–11805.
22 R. Wang, *Physiol. Rev.*, 2012, **92**, 791–896.
23 K. Abe and H. Kimura, *J. Neurosci.*, 1996, **16**, 1066–1071.
24 B. Y. Lv, S. L. N. Chen, C. S. Tang, H. F. Jin, J. B. Du and Y. Q. Huang, *J. Adv. Res.*, 2021, **27**, 85–97.
25 Y. Zhao and M. D. Pluth, *Angew. Chem., Int. Ed.*, 2016, **55**, 14638–14642.
26 F. A. Borges, B. D. Drago, L. O. Baggio, N. R. de Barros, G. S. P. Brasil, M. Scontri, C. U. Mussagy, M. C. D. Ribeiro, D. Milori, C. P. de Morais, B. S. Marangoni, G. Nicolodelli, M. Mecwan, K. Mandal, N. B. Guerra, C. R. Menegatti and R. D. Herculano, *Int. J. Biol. Macromol.*, 2022, **211**, 568–579.
27 T. Phaechamud, P. Issarayungyuen and W. Pichayakorn, *Int. J. Biol. Macromol.*, 2016, **85**, 634–644.
28 S. Chakrabarti, J. Islam, H. Hazarika, B. Mazumder, P. S. Raju and P. Chattopadhyay, *Cutaneous Ocul. Toxicol.*, 2018, **37**, 258–266.
29 H. S. Debone, P. S. Lopes, P. Severino, C. M. P. Yoshida, E. B. Souto and C. F. da Silva, *Int. J. Pharm.*, 2019, **555**, 146–152.
30 M. Gruppuso, G. Turco, E. Marsich and D. Porrelli, *Appl. Mater. Today*, 2021, **24**, 101148.
31 X. Y. Liu, Y. Q. Niu, K. C. Chen and S. G. Chen, *Mater. Sci. Eng. C*, 2017, **71**, 289–297.
32 Z. Y. Lan, R. Kar, M. Chwatko, E. Shoga and E. Cosgriff-Hernandez, *J. Biomed. Mater. Res., Part A*, 2023, **111**, 465–477.
33 X. Yang, W. Li, Y. Liu, N. Cao, Y. He, Q. Sun and S. Zhou, *Adv. Healthcare Mater.*, 2023, 2302183, DOI: **10.1002/adhm.202302183**.
34 C. Gao, L. Zhang, J. Wang, M. Jin, Q. Tang, Z. Chen, Y. Cheng, R. Yang and G. Zhao, *J. Mater. Chem. B*, 2021, **9**, 3106–3130.
35 Q. Hou, K. Liu, C. Lian, J. Liu, W. Wei, T. Qiu and H. Dai, *Biomacromolecules*, 2023, **24**, 3397–3410.
36 Y. P. Liang, J. H. He and B. L. Guo, *ACS Nano*, 2021, **15**, 12687–12722.
37 H. He, Z. Xiao, Y. Zhou, A. Chen, X. Xuan, Y. Li, X. Guo, J. Zheng, J. Xiao and J. Wu, *J. Mater. Chem. B*, 2019, **7**, 1697–1707.
38 R. N. Dong and B. L. Guo, *Nano Today*, 2021, **41** 101290.
39 N. Nguyen, Z. H. Lin, S. R. Barman, C. Korupalli, J. Y. Cheng, N. X. Song, Y. Chang, F. L. Mi, H. L. Song, H. W. Sung and Y. J. Lin, *Nano Energy*, 2022, **99**, 107393.
40 X. Xuan, Y. Zhou, A. Chen, S. Zheng, Y. An, H. He, W. Huang, Y. Chen, Y. Yang, S. Li, T. Xuan, J. Xiao, X. Li and J. Wu, *J. Mater. Chem. B*, 2020, **8**, 1359–1370.
41 S. Dhivya, V. V. Padma and E. Santhini, *Biomedicine*, 2015, **5**, 22.
42 L. Djekic, M. Martinovic, A. Ciric and J. Fraj, *Pharm. Dev. Technol.*, 2020, **25**, 332–339.
43 Y. X. Dong, M. H. Cui, J. Qu, X. C. Wang, S. H. Kwon, J. Barrera, N. Elvassore and G. C. Gurtner, *Acta Biomater.*, 2020, **108**, 56–66.
44 T. Hu, G. P. Wu, H. T. Bu, H. Y. Zhang, W. X. Li, K. Song and G. B. Jiang, *Chem. Eng. J.*, 2022, **450**, 138201.
45 J. Sun, X. Xie, Y. Song, T. Sun, X. Liu, H. Yuan and C. Shen, *Bioact. Mater.*, 2024, **35**, 495–516.
46 J. He, W. Zhang, Y. Cui, L. Cheng, X. L. Chen and X. Wang, *Adv. Healthcare Mater.*, 2024, 2303599.
47 Y. Huang, H. Li, X. He, X. Yang, L. Li, S. Liu, Z. Zou, K. Wang and J. Liu, *Chin. Chem. Lett.*, 2020, **31**, 787–791.
48 H. Ye, Y. Xian, S. Li, C. Zhang and D. Wu, *Biomater. Sci.*, 2022, **10**, 4218–4227.
49 K. Huang, W. Liu, W. Wei, Y. Zhao, P. Zhuang, X. Wang, Y. Wang, Y. Hu and H. Dai, *ACS Nano*, 2022, **16**, 19491–19508.
50 M. Z. Liu, H. Q. Zhang, D. H. Min, X. X. Miao, F. S. Li, L. N. Dong, J. J. Xing, G. H. Guo and X. L. Wang, *Mater. Sci. Eng., C*, 2019, **94**, 1077–1082.
51 K. Liu, Y. Kang, X. Dong, Q. Li, Y. Wang, X. Wu, X. Yang, Z. Chen and H. Dai, *Chem. Eng. J.*, 2023, **470**, 143987.
52 Y. Zhu, Q. Jiang, Z. Jin, D. Chen, Q. Xu, J. Chen, Y. Zeng, S. Chen and Q. He, *Adv. Healthcare Mater.*, 2023, **12**, 2201705.
53 S. Amadesi, C. Reni, R. Katare, M. Meloni, A. Oikawa, A. P. Beltrami, E. Avolio, D. Cesselli, O. Fortunato, G. Spinetti, R. Ascione, E. Cangiano, M. Valgimigli, S. P. Hunt, C. Emanueli and P. Madeddu, *Circulation*, 2012, **125**, 1774–1786.
54 S. D. Brain, *Immunopharmacology*, 1997, **37**, 133–152.
55 M. Toda, T. Suzuki, K. Hosono, Y. Kurihara, H. Kurihara, I. Hayashi, H. Kitasato, S. Hoka and M. Majima, *Biomed. Pharmacother.*, 2008, **62**, 352–359.
56 A. Hervera, F. De Virgiliis, I. Palmisano, L. M. Zhou, E. Tantardini, G. P. Kong, T. Hutson, M. C. Danzi, R. B. T. Perry, C. X. C. Santos, A. N. Kapustin, R. A. Fleck, J. A. Del Río, T. Carroll, V. Lemmon, J. L. Bixby, A. M. Shah, M. Fainzilber and S. Di Giovanni, *Nat. Cell Biol.*, 2018, **20**, 1098.
57 S. M. Wang, H. P. Tsai, J. J. Huang, H. C. Huang, J. L. Lin and P. H. Liu, *Exp. Neurol.*, 2009, **216**, 499–510.
58 D. Gero, R. Torregrossa, A. Perry, A. Waters, S. Le-Trionnaire, J. L. Whatmore, M. Wood and M. Whiteman, *Pharmacol. Res.*, 2016, **113**, 186–198.

59 Y. Jia, W. Yang, K. Zhang, S. Qiu, J. Xu, C. Wang and Y. Chai, *Acta Biomater.*, 2019, **83**, 291–301.
60 J. Qu, X. Zhao, Y. P. Liang, Y. M. Xu, P. X. Ma and B. L. Guo, *Chem. Eng. J.*, 2019, **362**, 548–560.
61 Y. Yuan, S. H. Shen and D. D. Fan, *Biomaterials*, 2021, **276**, 120838.
62 X. Liu, X. Han, Y. Shang, L. Wang, J. Shen and J. Yuan, *Int. J. Biol. Macromol.*, 2023, **253**, 127053.
63 Y. P. Liang, X. Zhao, T. L. Hu, B. J. Chen, Z. H. Yin, P. X. Ma and B. L. Guo, *Small*, 2019, **15**, 1900046.
64 B. Laverdet, A. Danigo, D. Girard, L. Magy, C. Demiot and A. Desmoulière, *Histol. Histopathol.*, 2015, **30**, 875–892.